CHEMISTRY
A EUROPEAN JOURNAL

DOI: 10.1002/chem.200800458

Controllable Synthesis of Zinc-Substituted α- and β-Nickel Hydroxide Nanostructures and Their Collective Intrinsic Properties

Bo Hu, Shao-Feng Chen, Shu-Juan Liu, Qing-Song Wu, Wei-Tang Yao, and Shu-Hong Yu*[a]

Abstract: A new controllable homogeneous precipitation approach has been developed to synthesize zinc-substituted nickel hydroxide nanostructures with different Zn contents from a zinc nanostructured reactant. As typical layered double hydroxides (LDHs), zinc-substituted nickel hydroxide nanostructures can be formulated as $NiZn_x(Cl)_y(OH)_{2(1+x)-y}\cdot z\,H_2O$ ($x=0.34$–0.89, $y=0$–0.24, $z=0$–1.36). The structure and morphology of zinc-substituted nickel hydroxide nanostructures can be systematically controlled by adjustment of the zinc content. The effects of temperature and the amounts of ammonia and zinc nanostructured precursor on the reaction were systematically investigated. In our new method, although zinc-substituted α-and β-nickel hydroxides have the typical 3D flower-like architecture and stacks-of-pancakes nanostructures, respectively, their growth processes are different from those previously reported. A coordinative homogeneous precipitation mechanism is proposed to explain the formation process of zinc-substituted nickel hydroxide nanostructures. The zinc-substituted nickel hydroxide nanostructures exhibit some interesting intrinsic properties, and changing the zinc content can effectively tune their optical, magnetic, and electrical properties.

Keywords: electrochemistry · hydrothermal synthesis · nanostructures · nickel hydroxide · zinc

Introduction

Nickel hydroxide as the cathode material of nickel-based rechargeable alkaline batteries,[1,2] such as nickel/cadmium (Ni/Cd), nickel/iron (Ni/Fe), nickel/metal hydride (Ni/MH), and nickel/zinc (Ni/Zn), is becoming more and more important in daily life.[3] Furthermore, some studies have focused on important optical and magnetic properties of nickel hydroxide compounds,[4] and hence nickel hydroxide is a potentially multifunctional material due to its useful electrical, optical, and magnetic properties.[5] Nickel hydroxide $Ni(OH)_2$ is a typical member of the large family of lamellar materials known as layered double hydroxides (LDHs) and has a hexagonal layered structure with two polymorphs, that is, α- and β-phases.[6] α-Nickel hydroxide has a brucite-like ($Mg(OH)_2$) structure with turbostratic disorder, and consists of stacked $Ni(OH)_{2-x}$ layers along the *c* axis intercalated with various anions or water molecules. The generally formulated composition is $Ni(OH)_{2-x}(A^{n-})_{x/n}\cdot y\,H_2O$, where $x=0.2$–0.4, $y=0.6$–1, and A = chloride, sulfate, nitrate, carbonate, or other anions.[7] In contrast, β-nickel hydroxide has a well-ordered brucite-like structure without any intercalated species,[8] and the layers are perfectly stacked along the *c* axis with an interlamellar distance of 4.6 Å. Therefore, the main structural analogy between α- and β-$Ni(OH)_2$ phases is stacking of $Ni(OH)_2$ layers along the *c* axis,[6] and the main difference is whether intercalated anions or water molecules are present or not.

Metal-substituted nickel hydroxides are made by partial substitution of Ni^{2+} ions in the nickel hydroxide layers by trivalent or divalent cations such as Zn,[8,9] Al,[10] Co,[4a,5] Fe,[11] and Mn,[12] among which zinc has been intensively studied. The main effects of zinc cations are prolonged stability in the KOH electrolytic medium[6] and preventing the formation of γ-NiOOH on overcharge in concentrated electrolyte.[5] However, other interesting intrinsic properties of zinc-substituted nickel hydroxide materials have rarely been reported. General techniques for their preparation include the co-precipitation method[6,13,14] and homogeneous precipi-

[a] Dr. B. Hu, S.-F. Chen, S.-J. Liu, Q.-S. Wu, W.-T. Yao, Prof. Dr. S.-H. Yu
Division of Nanomaterials and Chemistry
Hefei National Laboratory for Physical Sciences at Microscale
Structure Research Laboratory of CAS, Department of Chemistry
University of Science and Technology of China
Hefei, Anhui 230026 (China)
Fax: (+86) 0551-3603040
E-mail: shyu@ustc.edu.cn

Supporting information for this article is available on the WWW under http://dx.doi.org/10.1002/chem.200800458.

tation with hydrolysis of urea[11] or hexamethylenetetramine (HMT).[15] In the former method, although the metal-substituted nickel hydroxide could be routinely obtained by employing nickel salts, metal salts, and bases such as LiOH[13,14] and NaOH,[6] the resulting products have low crystalline quality[15] and hence poor reproducibility,[16] and they often require a subsequent hydrothermal process.[14] In the second method, although the homogeneous precipitation can be successfully controlled by the stepwise hydrolysis of urea or HMT to synthesize well-crystallized materials.[9a,15] no attempt has been made to provide another controllable method which can effectively achieve homogeneous precipitation.

Here, we report that zinc-substituted nickel hydroxide nanostructures can be synthesized by a new controllable method involving homogeneous precipitation in the presence of a nanostructured reactant and ammonia. The structure, morphology, and chemical composition of the zinc-substituted nickel hydroxide nanostructures can be effectively controlled by facile adjustment of the initial molar ratio of nickel salts to the reactant. The evolution process of the structure, morphology, and chemical composition of the products is investigated. Moreover, a coordinative homogeneous precipitation mechanism is proposed to explain the formation process of zinc-substituted nickel hydroxide nanostructures. As-synthesized zinc-substituted nickel hydroxide nanostructures exhibit some interesting intrinsic properties, and have potential as multifunctional materials due to their useful optical, magnetic, and electrical properties.

Results and Discussion

Structure and morphology analysis of zinc-substituted nickel hydroxide nanostructures

XRD analysis: X-ray diffraction showed that as-synthesized samples have undergone transformation from α-$Ni(OH)_2$ phase to β-$Ni(OH)_2$ phase. Figure 1 shows XRD patterns of the precursor and as-synthesized samples 1–5 obtained with the same amount of ammonia at different molar ratio of nickel salts to the zinc reactant by hydrothermal treatment at 120 °C for 12 h. The XRD pattern of the precursor in Figure 1 a corresponds to the well-crystallized $Zn_5(OH)_8Cl_2{\cdot}H_2O$ phase (JCPDS card number 72-0922) with a hexagonal lattice ($a=6.34$, $c=23.64$ Å). The XRD pattern of samples 1–3 (Figure 1 b–d) has the characteristic diffraction peaks of α-$Ni(OH)_2$ phase (JCPDS card number 38-0715). The values of $d(00i)$ are determined by the thickness of the brucite-like layer and the nature of the interlayer anions[17,18] The d_{003} value of sample 2 is 8.07 Å, which is larger than the literature value of 7.79 Å for the d spacing of $Ni(OH)_2$,[19,20] and such change in the d_{003} values could also be confirmed by HRTEM analysis.[6,13,21] Such a difference in spacing may correspond to the amounts of water and Cl^- anions intercalated between the octahedral $Ni(OH)_2$ layers, or to different amounts of zinc cations substituting for nickel cations in the $Ni(OH)_2$ layers.[6,8] The peaks in the XRD pattern of sample 5 (Figure 1 f) can be indexed as a hexagonal β-$Ni(OH)_2$ phase, in good agreement with standard values (JCPDS card number 74-2075). The XRD pattern of sample 4 (Figure 1 e) shows that the product consists of two well-known phases, that is, α-$Ni(OH)_2$ and β-$Ni(OH)_2$.

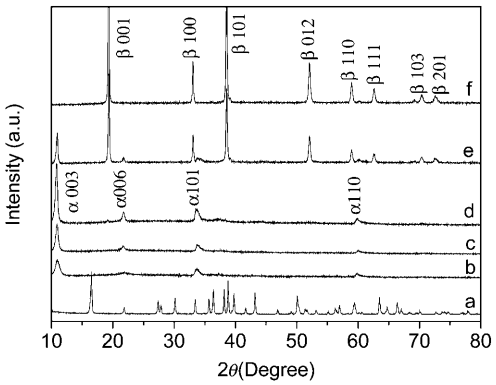

Figure 1. XRD patterns of a) the precursor $Zn_5(OH)_8Cl_2{\cdot}H_2O$ and samples synthesized by hydrothermal reaction of a solution comprising $Zn_5(OH)_8Cl_2{\cdot}H_2O$ (0.08 mmol), ammonia (3.5 mL; 25–28 wt %), and double-distilled water (42 mL) at 120 °C for 12 h with different amounts of $NiCl_2{\cdot}6H_2O$: b) 0.2 mmol (sample 1), c) 0.3 mmol (sample 2), d) 0.5 mmol (sample 3), e) 0.7 mmol (sample 4), and f) 0.9 mmol (sample 5). The experimental results are summarized in the Supporting Information, Table S1.

FTIR analysis: FTIR spectra further confirm that samples 2 and 5 are α-$Ni(OH)_2$ and β-$Ni(OH)_2$ phases, respectively (see Supporting Information, Figure S1). The FTIR spectra of sample 2 clearly shows vibrational bands that are typical of α-nickel hydroxide.[9b,22] Broadening of the band centered around 3450 cm^{-1} is due to the ν_{O-H} stretching vibrational mode of H-bonded water molecules located in the interlamellar space of the turbostratic structure of α-$Ni(OH)_2$.[6,9b] The band around 1630 cm^{-1} is attributed to the bending mode of the interlayer water molecules.[9b,16] The strong stretching vibrations in the region 1500–1000 cm^{-1} are due to intercalated anions (Cl^-).[16] The absorption at about 608 cm^{-1} is ascribed to the δ_{O-H} bending mode.[22,23] The absorptions at about 514 and 467 cm^{-1} can be assigned to $\delta_{Ni\text{-}O\text{-}H}$ bending and ν_{Ni-O} stretching modes, respectively.[9b] On the other hand, the FTIR spectrum of sample 5 shows vibrational bands at about 3636, 1630, 1382, and 516 cm^{-1}, as are typically observed for β-nickel hydroxide.[9b,16] A sharp peak at about 3636 cm^{-1} is due to stretching vibrations of non-hydrogen-bonded hydroxyl groups.[23] The band around 1630 cm^{-1} can be attributed to absorption of water molecules.[9b,16] Weak bands at about 1382 cm^{-1} are due to absorption of Cl^- anions at the surface of sample 5.[16] The band at about 516 cm^{-1} can be assigned to $\delta_{Ni\text{-}O\text{-}H}$ bending modes.[9b]

Thermogravimetric analysis (TGA): Both α- and β-nickel hydroxides undergo two-step weight loss, and α-nickel hydroxide has a larger mass loss than β-nickel hydroxide.[6,8]

The TGA curves of sample 2 and 5 show different net weight losses (see Supporting Information, Figure S2) of 28.76 and 20.70 wt%, respectively, for temperatures ranging from 25 to 600 °C. Sample 2 has a higher first-step weight loss than sample 5. The first-step weight loss of α-nickel hydroxide is classically attributed to the loss of both adsorbed water and part of the intercalated water,[6,8,9b] while β-nickel hydroxide just loses the absorbed water in the first step.[6]

Elemental analysis: From the elemental analyses (Table 1) and TGA curves of the samples, it can be seen that small parts of the anions and water molecules are intercalated in

Table 1. Elemental analysis data of samples 1–5.

Sample	Ni [wt%]	Zn [wt%]	Cl [wt%]	Total [wt%]	Chemical composition
1	48.72	48.33	2.95	100	$NiZn_{0.89}(OH)_{3.68}Cl_{0.1}(H_2O)_{1.36}$
2	50.21	44.73	5.06	100	$NiZn_{0.80}(OH)_{3.43}Cl_{0.17}(H_2O)_{1.16}$
3	50.17	42.58	7.25	100	$NiZn_{0.76}(OH)_{3.28}Cl_{0.24}(H_2O)_{1.24}$
4	63.50	34.67	1.83	100	$NiZn_{0.49}(OH)_{2.93}Cl_{0.05}(H_2O)_{0.74}$
5	72.80	27.20	0	100	$NiZn_{0.34}(OH)_{2.68}$

the interlayers of α-$Ni(OH)_2$. More importantly, zinc cations have successfully substituted part of the nickel cations in the nickel hydroxide nanostructures. On the basis of the result of TGA analysis and elemental analysis, the chemical composition of the samples can be formulated (Table 1). In our experiments, the initial molar ratio of nickel cations to zinc cations for samples 1–5 are 2:4, 3:4, 5:4, 7:4, and 9:4, respectively. Thus, compared with the initial molar ratio of nickel cations to zinc cations, the final ratio of the two ions in the zinc-substituted nickel hydroxide samples shows a gradual change from sample 1 to sample 5. For samples 1 and 2, some of the zinc cations fail to take part the reaction. For sample 3, the two ions react with each other completely. For samples 4 and 5, the same nickel cations are not involved in the reaction. These results demonstrate that a series of zinc-substituted nickel hydroxide nanostructures with different Zn contents can be synthesized by using this facile method. The general molecular formula can be summarized as $NiZn_x(Cl)_y(OH)_{2(1+x)-y}\cdot z\,H_2O$ ($x = 0.34$–0.89, $y = 0$–0.24, $z = 0$–1.36).

Morphological analysis: The nanostructured zinc precursor and zinc-substituted nickel hydroxide nanostructures have interesting morphological characteristics. Figure 2a shows an SEM image of a typical reactant composed of many hexagonal nanoflakes. Figure 2b and c show that sample 2 consists of uniform 3D flowerlike nanostructures. Clearly, the entire structure is built from dozens of nanosheets with smooth surface. These smooth nanosheets are 20–30 nm thick and 0.6–2.0 μm wide, and they are connected to each other randomly to form 3D flowerlike nanostructures. The selected-area electron diffraction (SAED) pattern recorded along the [001] zone axis shows a typical single-crystalline nature (Figure 2e), which is similar to that of the hexagonal

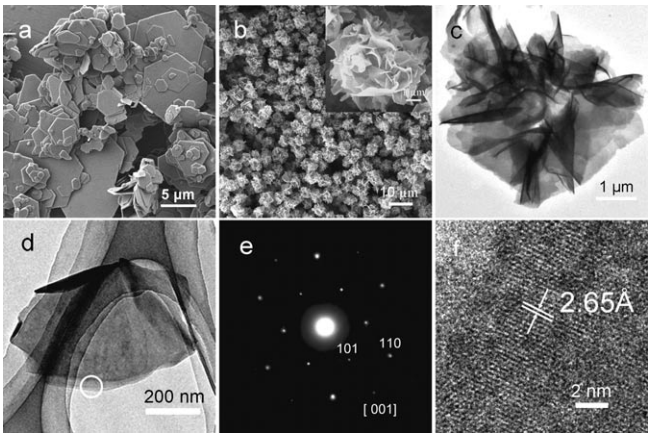

Figure 2. SEM images of a) the reactant and b) sample 2. c) TEM image of sample 2. d) TEM image of a single nanosheet, obtained by strong supersonic vibration of the sample prior to preparation for TEM analysis. e) A typical electron diffraction pattern taken on a piece of extended nanosheet of the flowerlike nanostructure along the [001] direction. f) HRTEM image of the structure.

α-$Ni(OH)_2$ phase. A lattice-resolved HRTEM image (Figure 2f) shows an interlamellar spacing of about 2.65 Å, which corresponds to the lattice spacing of the (101) plane.

Figure 3a–c show that sample 5 is composed of "stacks-of-pancakes" nanostructures[24] which are formed from nanosheet building blocks with layer-by-layer stacking structure.

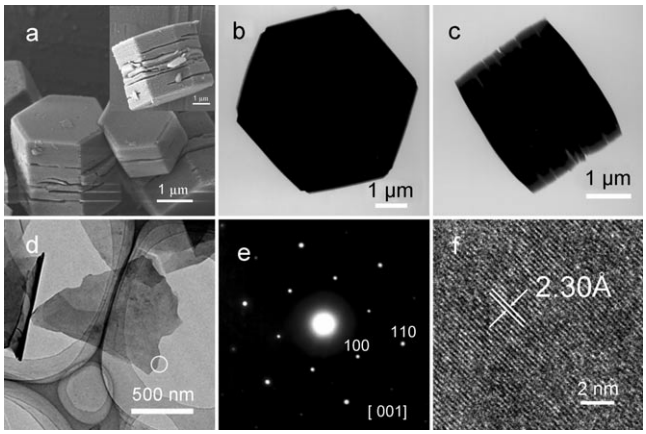

Figure 3. a) SEM image and b and c) TEM images of sample 5. d) TEM image of a typical single sheet, obtained by strong ultrasonic treatment of the sample prior to preparation for TEM analysis. e) A typical selected-area electron diffraction pattern taken on a piece of extended nanosheet of the nanoflower along the [001] direction. f) HRTEM image taken on the selected area in d).

The SAED pattern (Figure 3e), which can be attributed to [001] zone axis diffraction, suggests that the stacks-of-pancakes structure is a single crystal, close to the hexagonal β-$Ni(OH)_2$ phase. A representative HRTEM image (Figure 3f) shows that lattice fringes are structurally uniform with a lattice spacing of 2.30 Å, which is good agreement with the *d* value of the (002) plane of the hexagonal β-

$Ni(OH)_2$ phase, that is, stacks of the hierarchical structure have a preferential [001] growth direction. The above characterization data indicate that both the zinc-substituted α-$Ni(OH)_2$ flowerlike structure and zinc-substituted β-$Ni(OH)_2$ stacks-of-pancakes structure are built from nanosheets that are single-crystalline and have identical crystal orientation. Samples 1 and 3 have similar 3D flowerlike nanostructures to sample 2, and sample 4 has not only 3D flowerlike nanostructures, but also some hexagonal sheets (see Supporting Information, Figure S3). Thus, the samples undergo a morphological evolution process from 3D flowerlike architectures to stacks-of-pancakes nanostructures with decreasing zinc content.

Formation process of zinc-substituted nickel hydroxide nanostructures

Effect of temperature: Temperature plays a critical role in this new synthetic method. For example, when other reaction conditions for synthesis of sample 2 are kept constant, temperature has significant influence on the structure and morphology. In the range of 80–120 °C, the samples can be indexed as α-nickel hydroxide (Figure 4a, b and Figure 1c)

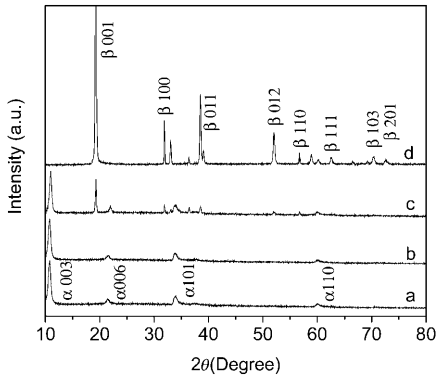

Figure 4. XRD patterns of samples prepared by hydrothermal reaction of a solution comprising $NiCl_2{\cdot}6H_2O$ (0.3 mmol), $Zn_5(OH)_8Cl_2{\cdot}H_2O$ (0.08 mmol), ammonia (3.5 mL; 25–28 wt%), and double-distilled water (42 mL) for 12 h at different temperatures: a) 80 (sample 6), b) 100 (sample 7), c) 140 (sample 8), d) 160 °C (sample 9).

and have 3D flowerlike nanostructures (see Supporting Information, Figures S4a, b and Figure 2). When the temperature increases to 140 °C, a mixed product made of α-$Ni(OH)_2$ and β-$Ni(OH)_2$ phases is obtained (Figure 4c). The SEM image (see Supporting Information, Figure S4c) shows that the final product includes not only 3D flowerlike architectures, but also hexagonal nanosheets. However, when the temperature rises to 160 °C, the XRD pattern (Figure 4d) clearly reveals that the well-crystallized β-nickel hydroxide phase and hexagonal ZnO phase (JCPDS card number 05-0664) are formed. The SEM image shows two different morphologies of hexagonal nanosheets and hexagonal rods (see Supporting Information, Figure S4d).

Effect of the initial amount of ammonia: Further studies revealed the key role of the initial amount of ammonia in this new synthetic method. Previously, addition of ammonia to the aqueous reaction system was reported to largely increase the solubility of the reactant.[25] Besides, ammonia displays strong propensity for complexation of nickel cations.[24] While the other reaction conditions for the synthesis of sample 2 were kept constant, six experiments were performed with different amounts of ammonia. In a control experiment without adding ammonia, the final products were the $Zn_5(OH)_8Cl_2{\cdot}H_2O$ phase and well-crystallized ZnO phase, as confirmed clearly by the XRD pattern (Figure 5a).

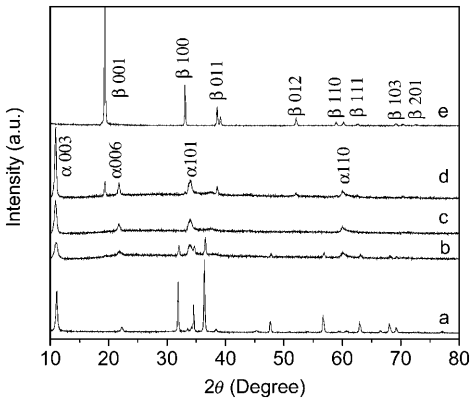

Figure 5. XRD patterns of samples prepared by hydrothermal reaction of a solution comprising $NiCl_2{\cdot}6H_2O$ (0.3 mmol), $Zn_5(OH)_8Cl_2{\cdot}H_2O$ (0.08 mmol), and double-distilled water (42 mL) at 120 °C for 12 h with different amounts of ammonia (25–28 wt%): a) 0 (sample 10), b) 2.5 (sample 11), c) 4.5 (sample 12), d) 5.5 (sample 13), e) 6.5 mL (sample 14).

Hexagonal rods and irregular plates are obtained, and the plates have some large or small holes at the surface (see Supporting Information, Figure S5a). Therefore, when no ammonia coordinates to the reactant and nickel cations to form complexes, only part of the reactant dissolves to form ZnO hexagonal nanorods, and the nickel cations do not participate in the reaction. When the amount of ammonia is increased to 2.5 mL, the XRD pattern (Figure 5b) indicates that the products are α-$Ni(OH)_2$ and ZnO phases. Flowerlike 3D nanostructures and hexagonal rods are formed (see Supporting Information, Figure S5b). With amounts of ammonia of 3.5, 4.5, and 5.5 mL, the samples are still α-nickel hydroxide phase, as shown in Figures 1c and 5c, d, and all particles have similar 3D flowerlike nanostructures (see Supporting Information, Figure S5c–e). However, once the amount of ammonia is increased to 6.5 mL, the well-crystallized β-nickel hydroxide phase forms (Figure 5e) and has the stacks-of-pancakes morphology[24] (see Supporting Information, Figure S5f).

Effect of the nanostructured zinc precursor: The nanostructured zinc precursor plays a crucial role in the formation of the zinc-substituted nickel hydroxide structures. When the initial amount of nickel cations is 0.3 mmol, 3D flowerlike

α-nickel hydroxide nanostructures are formed. In contrast, using the same molar amount of zinc salts such as $ZnCl_2$ instead of the zinc nanostructured precursor, and keeping other conditions constant, gives hexagonal nanosheets with a diameter of about 1 μm and an approximate thickness of 200 nm (Figure 6), and the product is a mixture of β-

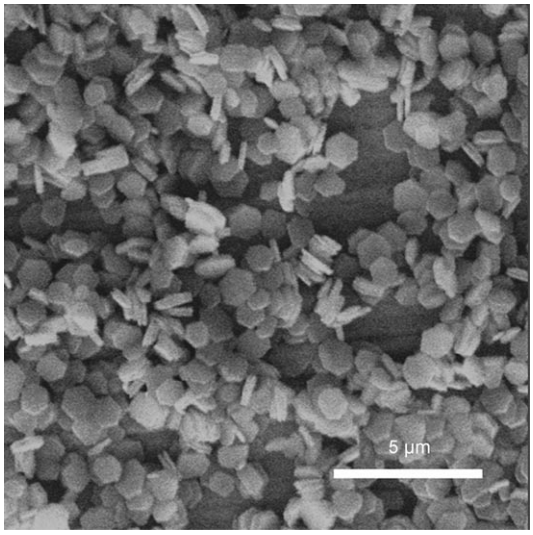

Figure 6. SEM image of sample 15 prepared by hydrothermal reaction of a solution comprising $NiCl_2{\cdot}6H_2O$ (0.3 mmol), $ZnCl_2$ (0.08 mmol), ammonia (3.5 mL; 25–28 wt%), and double-distilled water (42 mL) in 120°C for 12 h.

$Ni(OH)_2$ phase and ZnO phase, as confirmed by XRD analysis (see Supporting Information, Figure S6).

Formation process of zinc-substituted β-nickel hydroxide nanostructures: To elucidate the formation process of stacks of pancakes of the zinc-substituted β-nickel hydroxide nanostructures, time-dependent experiments were performed. The morphological evolution proceeds from α-$Ni(OH)_2$ nanosheets to intermediate α-$Ni(OH)_2$ hexagonal platelets and finally to β-$Ni(OH)_2$ stacks-of-pancakes architectures. When the hydrothermal reaction proceeds at 120°C for 0.5 h, as-synthesized nanosheets connect to each other to form flowerlike particles which are the reaction precursors of the LDH phase (Figure 7a). The XRD pattern in Figure 8a shows that only pure α-$Ni(OH)_2$ phase is obtained, but its crystallinity is poor. As the reaction proceeds, some hexagonal platelets form and connect to generate flowerlike architectures composed of many interlinked nanosheets (Figure 7b and Figure S7a–c, Supporting Information). The hexagonal platelets may be formed by a transformation process of the nanosheets. The XRD pattern in Figure 8b agrees well with the standard XRD pattern for α-$Ni(OH)_2$ phase.

After 4 h of reaction, hexagonal columns are present and some nanosheets connect with them (Figure 7c and Figure S7d, Supporting Information). Simultaneously, some flowerlike nanostructures which connect to the hexagonal columns decompose more completely. Thus, flowerlike nanostructures can be seen to gradually change into hexagonal columns. The XRD pattern in Figure 8c shows that α-$Ni(OH)_2$ and β-$Ni(OH)_2$ phases coexist. The appearance of β-$Ni(OH)_2$ phase may correspond to the thickening process of hexagonal platelets. When the reaction time is 8 h, hexagonal column morphology is exclusively present and the flowerlike nanostructures have disappeared (Figure 7d). The XRD pattern (Figure 8d) matches well with that of pure β-$Ni(OH)_2$ phase. Finally, when the reaction time is prolonged to 12 h, the sample is composed entirely of the stacks-of-

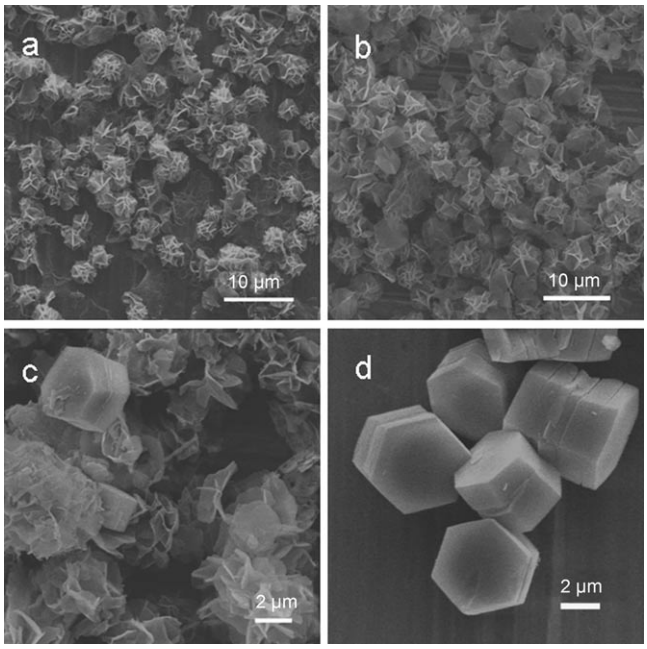

Figure 7. SEM images of samples prepared by hydrothermal reaction of a solution comprising $NiCl_2{\cdot}6H_2O$ (0.9 mmol), $Zn_5(OH)_8Cl_2{\cdot}H_2O$ (0.08 mmol), ammonia (3.5 mL; 25–28 wt%), and double-distilled water (42 mL) in 120°C for different reaction periods: a) 0.5 (sample 16), b) 2 (sample 17), c) 4 (sample 18), d) 8 h (sample 19).

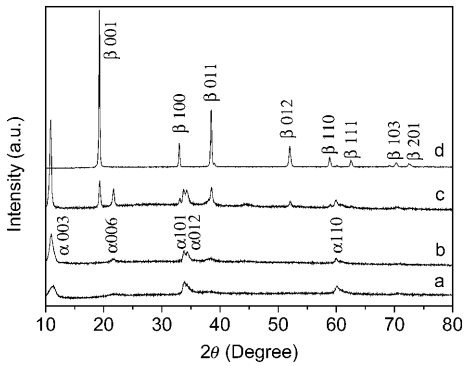

Figure 8. XRD patterns of samples prepared by hydrothermal reaction of a solution comprising $NiCl_2{\cdot}6H_2O$ (0.9 mmol), $Zn_5(OH)_8Cl_2{\cdot}H_2O$ (0.08 mmol), ammonia (3.5 mL; 25–28 wt%), and double-distilled water (42 mL) at 120°C for different reaction periods: a) 0.5 (sample 16), b) 2 (sample 17), c) 4 (sample 18), d) 8 h (sample 19).

pancakes morphology of the pure β-$Ni(OH)_2$ phase (Figures 3, 1 f).

Formation process of zinc-substituted α-nickel hydroxide nanostructures: In the case of the flowerlike zinc-substituted α-nickel hydroxide nanostructures, the time-dependent shape-evolution process was examined while the initial amount of nickel cations was kept at 0.3 mmol. After hydrothermal reaction at 120 °C for 0.5 h, nanosheets that are flexible and randomly bent (see Supporting Information, Figure S8a, e, f) form and connect with each other. The nanosheets consist of pure α-$Ni(OH)_2$ phase (see Supporting Information, Figure S9a), and the d_{003} value for the interlayer distance is about 7.54 Å. As the reaction time is prolonged up to 2, 4, and 8 h, the 3D architectures grow gradually and some flowerlike morphology appears (see Supporting Information, Figure S8b–d). Simultaneously, pure α-$Ni(OH)_2$ phase is formed (see Supporting Information, Figure S9b–d) and the d_{003} values are about 7.66 Å, 7.99 Å, and 8.01 Å, respectively. When the reaction time is prolonged to 12 h, the resulting sample 2 is composed entirely of 3D flowerlike nanostructures (Figure 3) of pure α-$Ni(OH)_2$ phase with a d_{003} value of about 8.07 Å (Figure 1 c).

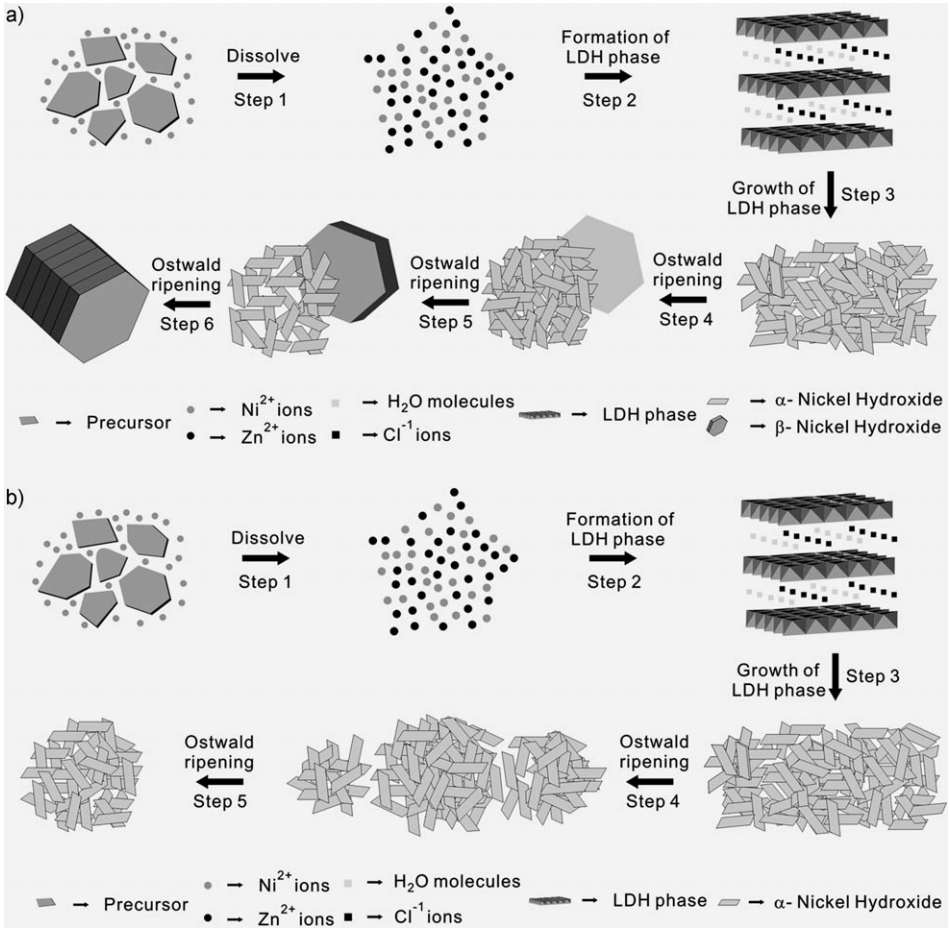

Figure 9. Schematic illustration of the morphological evolution of zinc-substituted β-nickel hydroxide nanostructures (a) and zinc-substituted α-nickel hydroxide nanostructures (b).

Formation mechanism of zinc-substituted nickel hydroxide nanostructures

Morphological evolution process: On the basis of the above results, the scheme illustrated in Figure 9 a is proposed for growth process of zinc-substituted β-nickel hydroxide nanostructures. Such a process is different from those reported earlier. Hochepied et. al[24] described a mechanism involving oriented attachment of platelets in perfect parallel orientation with respect to one another and partial recrystallization in the core of the particles leading to β-$Ni(OH)_2$ stacks-of-pancakes morphology. Zhu et. al[21] reported the formation of nickel hydroxide nanocolumns by stacking of oriented $Ni(OH)_2$ nanosheets.

In our experiments, ammonia can act as a ligating agent for nickel cations and the reactant to form complexes. The complexes are stable in alkaline systems at ambient temperature, but as the temperature increases, their stability decreases.[25] In the second growth stage, reaction of OH^- with the complex could cause the bonds between the nickel cations and ammonia to become weaker and bonds between Ni^{2+} and OH^- to form gradually at the reaction temperature. The initially precipitated $Ni(OH)_2$ may dissolve and incorporate zinc cations.[15] At the same time, when zinc cations substitute nickel cations in the nickel hydroxide layers, the anions (Cl^-) and/or molecular water are intercalated in the layers, and zinc-substituted LDH phase is formed. In the third step, based on a self-assembly process, the LDH phases develop by stacking along the *c* axis to yield the final nanosheets. In step 4, due to the effect of Ostwald ripening, the sample changes from α-$Ni(OH)_2$ nanosheets to α-$Ni(OH)_2$ hexagonal platelets, because the hexagonal platelets are thermodynamically stable and can easily be synthesized. In step 5, more and more α-$Ni(OH)_2$ nanosheets are transformed, and the α-$Ni(OH)_2$ hexagonal platelets become thicker and grow gradually into hexagonal columns. At the same time, the hexagonal columns change from α-$Ni(OH)_2$ phase to β-$Ni(OH)_2$ phase. In step 6, the α-$Ni(OH)_2$ nanosheets totally disappear, and the hexagonal columns consist of pure β-$Ni(OH)_2$ phase. Finally, β-

$Ni(OH)_2$ hexagonal columns turn into the β-$Ni(OH)_2$ stacks-of-pancakes morphology, in which hexagonal platelets have perfect parallel orientation with respect to each other other.[24]

The whole growth process of zinc-substituted α-nickel hydroxide nanostructures is summarized in Figure 9b. However, such a process is neither consistent with previous reports on 3D flowerlike structures from a so-called two-stage growth process consisting of fast nucleation of amorphous primary particles followed by slow aggregation and crystallization of primary particles,[26] nor with the report by Li et al. on a one-step self-assembly process leading to spherelike α-$Ni(OH)_2$, in which HMT acts as the nucleation center and helps to form the $Ni(OH)_2$ gel.[27] In the case of the flowerlike zinc-substituted α-nickel hydroxide nanostructures, the growth process is similar to that of the stacks-of-pancakes zinc-substituted β-nickel hydroxide nanostructures. First, the nickel cations and the reactant form complexes with ammonia; then, with increasing time, the zinc-substituted LDH phase and nanosheets consisting of pure α-$Ni(OH)_2$ phase gradually form. Finally, nanosheets form and connect to each other generate 3D flowerlike architectures, due to Ostwald ripening in terms of the principle of minimal structural change.[23] In the whole process of morphology evolution, the samples are always pure α-$Ni(OH)_2$ phase.

Formation mechanism of zinc-substituted nickel hydroxide nanostructures: Layered double hydroxides can be formed from aqueous solutions by coprecipitation and homogeneous precipitation methods.[28] The co-precipitation mechanism is determined by the rate of dissolution of the individual hydroxides, while the homogeneous precipitation method is controlled by the formation of heteronuclear hydroxo precursor complexes.[28] Homogeneous nucleation of zinc-substituted LDHs takes place with slow decomposition of the complex, and the rate of decomposition of the complex is a critical variable in the homogeneous nucleation process. In previous reports, only the rate of hydrolysis could compete favorably with homogeneous formation of the hydroxo precursor.[28] In our experiments, the reactant and nickel cations first form complexes with ammonia that can gradually decompose under hydrothermal conditions. Thus, we propose a new mechanism, called the coordinative homogeneous precipitation mechanism, in which the rate of decomposition of the complex determines the homogeneous nucleation of the zinc-substituted LDHs.

To further elucidate the coordinative homogeneous precipitation mechanism, we systemically studied the evolution of the chemical composition of the products. In the case of zinc-substituted α-nickel hydroxide nanostructures, energy-dispersive X-ray (EDX) spectra (see Supporting Information, Figure S10 and Table S2) show that not only different areas of the same nanosheet have the same atomic percentages of nickel and zinc, but also the same atomic percentages of nickel and zinc are found in different nanosheets. Therefore, the chemical composition of the samples further confirms that the homogeneous nucleation process takes place in the initial stage and forms zinc-substituted LDHs. For reaction times from 0.5 to 12 h, the EDX data suggest that the atomic percentage of zinc samples gradually undergoes a slight decrease (Table 2 and Supporting Information, Figure S11). This may be due to some of the unstable zinc cations in the structure dissolving during the Ostwald ripening process.

Table 2. EDX data of samples prepared by hydrothermal reaction of a solution comprising $NiCl_2·6H_2O$ (0.3 mmol), $Zn_5(OH)_8Cl_2·H_2O$ (0.08 mmol), ammonia (3.5 mL; 25–28 wt%), and double-distilled water (42 mL) at 120°C for different reaction times: 0.5 (sample 20), 2 (sample 21), 4 (sample 22), 8 (sample 23), and 12 h (sample 2).

Sample	Morphology	Ni [atom%]	Zn [atom%]
20	nanosheets	65.76	34.24
21	nanosheets and flowerlike nanostructures	65.61	34.39
22	nanosheets and flowerlike nanostructures	68.07	31.93
23	nanosheets and flowerlike nanostructures	69.66	30.34
2	flowerlike nanostructures	71.38	28.62

In the case of zinc-substituted β-nickel hydroxide nanostructures, EXD analysis was performed on nanosheets, hexagonal sheets, hexagonal columns, and stacks-of-pancakes structures for reaction times from 0.5 to 12 h. The EDX data showed that the nanosheets show a small increase in nickel atomic percentage and a slight decrease in zinc atomic percentage with increasing time (Table 3 and Supporting Information, Figure S12). In the same time period, the hexagonal sheets, hexagonal columns, and stacks of pancakes also show a slight increase in the nickel atomic percentage and correspondingly a small decrease in zinc atomic percentage. However, for a given sample, the nickel atomic percentage of the nanosheets is slightly larger than those of the hexagonal sheets, hexagonal columns, and stacks of pancakes. A detailed explanation of the changes in chemical composition during the time-dependent evolution process is under further exploration.

Table 3. EDX data of samples 16–19 and 5.

Sample	Morphology	Ni [atom%]	Zn [atom%]	Morphology	Ni [atom%]	Zn [atom%]
16	nanosheets	73.55	26.45			
17	nanosheets	73.13	26.87	hexagonal sheets	71.80	28.20
18	nanosheets	76.24	23.76	hexagonal columns	73.44	26.56
19				stacks-of-pancakes structures	80.68	19.32
5				stacks-of-pancakes structures	86.97	13.03

Chemical and physical properties of zinc-substituted nickel hydroxide nanostructures

BET surface area: Because of the novel 3D hierarchical structures of the zinc-substituted nickel hydroxide nanostructures, we determined their specific surface areas by BET measurements on an ASAP-2000 surface-area analyzer (see Supporting Information, Figure S13 for nitrogen adsorption/desorption isotherms). The BET surface areas of samples 1–5, calculated from nitrogen adsorption isotherms, are 73.425, 70.296, 42.209, 25.808, and 1.046 $m^2 g$, respectively. Thus, the 3D flowerlike structures of samples 1 and 2 have greater BET surface areas than the stacks-of-pancakes nanostructures of sample 5. Furthermore, from sample 1 to sample 5, the Zn content gradually decreases from 48.33 to 27.20%, while the BET surface areas decreases from 73.43 to 1.046 $m^2 g$. Therefore, the lower the Zn content, the lower BET surface area of the sample.

Chemical stability: The chemical stability of zinc-substituted nickel hydroxide samples in strongly alkaline medium was determined by powder XRD measurement after immersion of samples in 6 M KOH solution at room temperature for 40 d. The XRD patterns in Figure 10a and b indicate that

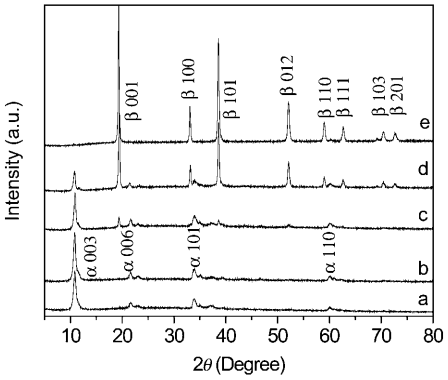

Figure 10. XRD patterns of samples immersed in 6 mol L^{-1} KOH solution for forty days. a–e) Samples 1–5, respectively.

post-treatment samples 1 and 2 are also α-$Ni(OH)_2$ phase with characteristic diffraction peaks around 8 Å and a broad asymmetric band at about 2.66 and 1.54 Å. The new peaks corresponding to $d = 3.86$ and 2.56 Å can also be indexed as the diffractions of α-$Ni(OH)_2$ phase due to disorder of the LDH.[6] These results indicate that the structure of zinc-substituted α-$Ni(OH)_2$ samples can be made more disordered in strongly alkaline medium. The XRD patterns in Figure 10c and for samples 3 and 4 after treatment correspond to α- and β-$Ni(OH)_2$ phases. The XRD pattern in Figure 10e shows that sample 5 after treatment remains the β-$Ni(OH)_2$ phase, consistent with a previous report.[9a]

To our knowledge, the zinc-substituted materials, especially α-$Ni(OH)_2$ phase (samples 1 and 2), have superior chemical stability in alkaline medium. On the basis of literature reports,[9a,b] we believe that this high stability may be attributed to the substitution of zinc cations. Tessier et al.[9a] reported that the presence of zinc cations in tetrahedral sites of the interslab space links the successive slabs, increases structural cohesion, and improves the electrochemical properties of the nickel hydroxide electrodes. This property could make this material more suitable as a positive electrode in alkaline batteries.

Optical properties: UV/Vis/NIR absorption spectra (Figure 11) with the incident light aligned perpendicular to the samples show that samples 1–5 have similar absorption

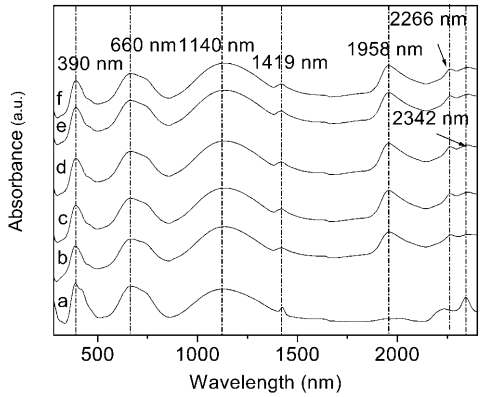

Figure 11. UV/Vis/NIR absorption spectra of a) sample 24 prepared by hydrothermal reaction of a solution comprising $NiCl_2 \cdot 6H_2O$ (0.3 mmol), ammonia (3.5 mL; 25–28 wt%), and double-distilled water (42 mL) at 120 °C for 12 h. b–f) Samples 1–5, respectively.

characteristics with absorption peaks centered at 390, 660, 1140, 1420, 1958, 2266, and 2353 nm. Thus, the ultraviolet (100–400 nm), visible (400–760 nm), and near-infrared (76o–5600 nm) regions all have absorption peaks. Sample 24, which is pure β-$Ni(OH)_2$ phase of irregular morphology (see Supporting Information, Figure S14a,b) without any Zn content, has a different absorption spectrum (Figure 11a), in which the peaks centered at 1958 and 2226 nm are absent and the peak centered at 2342 nm is stronger.

The room-temperature photoluminescence (PL) spectrum of the samples are depicted in Figure 12. The PL spectrum of sample 1 (Figure 12a) displays a strong green emission peak centered at 555 nm (2.23 eV). Sample 2 has a weak blue emission peak centered at 440 nm (2.82 eV) and a strong green emission peak centered at 500 nm (2.48 eV) (Figure 12b), sample 3 has a strong blue emission peak centered at 440 nm (2.82 eV; Figure 12c), and samples 4 and 5 (Figure 12d and e) display similar PL spectra with strong blue emission peaks centered at 440 nm (2.82 eV) and weak purple emission peaks centered at 418 nm (2.97 eV). Importantly, the PL spectra of zinc-substituted nickel hydroxide samples 1–5 are dependent on Zn content. They show blue-shifts over a large range from 555 to 418 nm with decreasing Zn content (from 48.33 to 27.20% in samples 1–5, respectively). In comparison, sample 24 has a strong blue emission

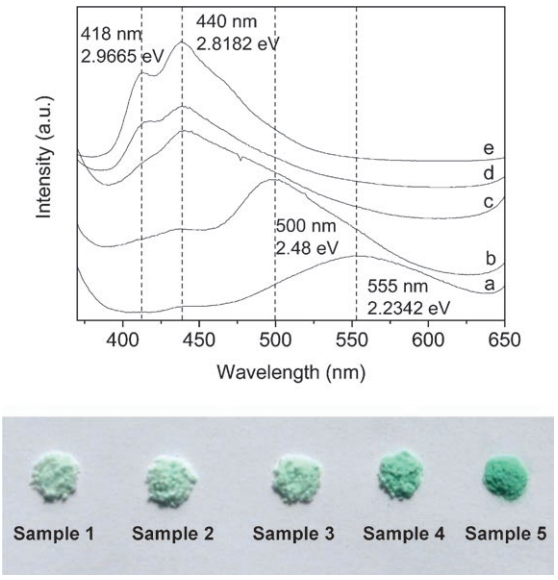

Figure 12. Top: PL spectra at 295 K of a–e) samples 1–5, respectively. The excitation wavelength was 340 nm. Bottom: Optical photographs of samples 1–5.

peak centered at 440 nm (2.8182 eV) and weak purple emission peaks centered at 406 nm (3.0542 eV; see Supporting Information, Figure S14c). In addition, optical photographs of samples 1–5 show gradual color changes from the azure to green (Figure 12).

To the best of our knowledge, the optical properties of zinc-substituted nickel hydroxide nanomaterials have rarely been reported so far. Delmas et al. reported that UV/Vis absorption bands of cobalt-substituted nickel hydroxide are related to the nickel and cobalt ions, as well as to the valences of the ions.[4a,b,29] Similarly, in our experiment, the UV/Vis/NIR absorption spectra of the samples are related to the nickel or zinc ions and their valence. As a result, the samples display similar absorption characters, and the Zn^{2+} ions are in the high-spin state and correspond to the 1958 and 2226 nm optical transitions. Furthermore, the complicated PL spectra of samples may result from the structure, morphology, and structural defects due to substituent zinc ions and intercalated anions or water. More details of the mechanism behind the optical spectra of the samples need to be elucidated in future.

Magnetic properties: Figure 13 shows temperature-dependent magnetization curves of the samples 1, 2, and 5 measured from 2 to 80 K with an external magnetic field of 100 Oe. Samples 1 and 2 exhibit the same magnetic behavior, with a critical temperature of about 8 K. Sample 5 has a critical temperature of about 20 K. Figure 14 shows the isothermal magnetization loops measured at 4 K on a commercial SQUID magnetometer for samples 1, 2, and 5. The hysteresis loops of samples 1 and 2 are similar and indicate ferromagnetic behavior. The coercivities of samples 1 and 2 are 58 and 83 Oe, respectively. The hysteresis loop of sample 5 shows antiferromagnetic behavior.

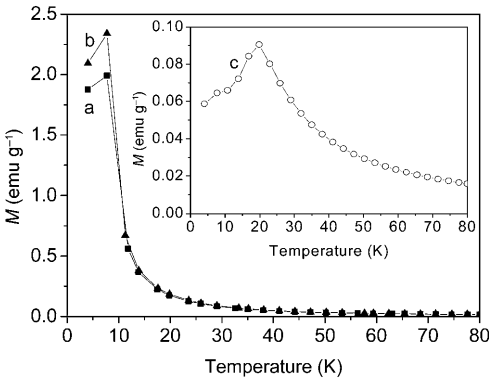

Figure 13. Temperature-dependent magnetization of samples with an external magnetic field of 100 Oe. a) sample 1 (■), b) sample 2 (▲), and c) sample 5 (○).

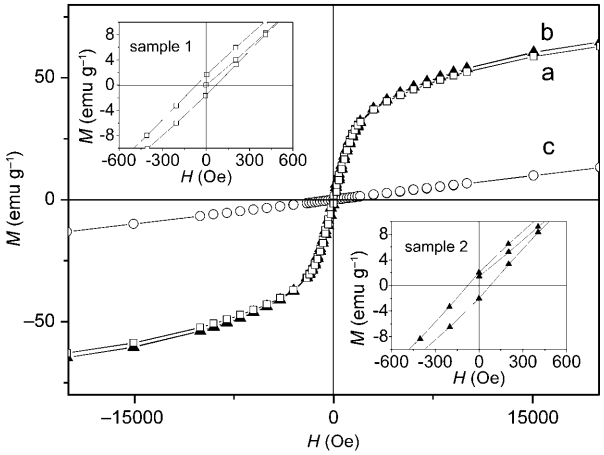

Figure 14. Isothermal magnetization at 4 K for a) sample 1 (□), b) sample 2 (▲), and c) sample 5 (○); the top-left inset shows the magnified isothermal magnetization at 4 K for sample 1; the bottom-right insert shows the magnified isothermal magnetization at 4 K for sample 2.

The magnetic properties of the α- and β-$Ni(OH)_2$ materials are highly dependent on the structure, morphology, magnetization direction, and the *d* spacing of the sample.[30,31] Samples 1 and 2 consist of pure α-$Ni(OH)_2$ phase and their magnetic properties with ferromagnetic order below 8 K are similar. Such a magnetic character is in good agreement with the magnetic behavior of α-$Ni(OH)_2$.[4c,d,32] Apparently, for samples 1 and 2 with the same d_{003} spacing of 8.07 Å, through-space dipole–dipole interaction between layers becomes predominant and favors long-range ferromagnetic order.[4c,d,33] Furthermore, samples 1 and 2 have a low coercive field at 4 K, which may be ascribed to the synergy effect of crystallinity, shape, surface, and single-ion anisotropies.[4c] Sample 5 consists of pure β-$Ni(OH)_2$ phase and its magnetic properties show antiferromagnetic order below 20 K, which is typically observed for β-$Ni(OH)_2$.[4d] Furthermore, for sample 5 with $d_{003} = 4.6$ Å, superexchange interaction occurs because of hydrogen bonding and may lead to antiferromagnetic order.[4e,30,31] Therefore, the magnetic properties of the

samples are closely related to the structural features, and the model of ferromagnetic layers interacting through dipolar coupling can interpret well the magnetic behavior of zinc-substituted nickel hydroxide nanostructures. Thus, it is possible to flexibly control the magnetic behavior by carefully changing the structure of zinc-substituted nickel hydroxide nanostructures, and this could be useful both in fundamental research and future magnetic devices.

Electrochemical properties: Zinc-substituted nickel hydroxide nanostructures have interesting electrochemical properties as electrode materials. Figure 15 shows the 10th cyclic

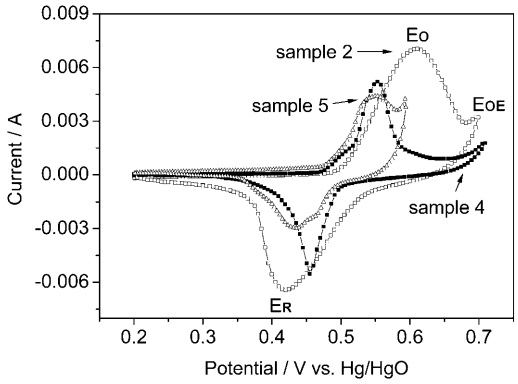

Figure 15. Cyclic voltammograms of zinc-substituted nickel hydroxide electrodes made from samples 2 (□), 4 (■), and 5 (△) at 20 °C and a scan rate of 1.5 mV s^{-1}.

voltammograms of the samples as electrodes at a potential scanning rate of 1.5 mV s^{-1}. Although the samples all have reversible peaks, their characteristics are different. The reason for this is unclear, but it may be due to structural and morphological changes, since zinc-substituted nickel hydroxide samples 2, 4, and 5 have different Zn contents of 44.73, 34.67, and 27.20 %, respectively. Table 4 shows the effects of Zn content on the oxidation potential E_O, oxygen-evolution potential E_{OE}, and reduction potential E_R. The decrease in Zn content from sample 2 to sample 5 reduces the E_O of the electrodes and the intensities of E_O and E_R. The differences E_O-E_R can characterize the reversibility of the electrode reaction, and smaller values imply more electrode reversibility.[3,7] The E_O-E_R data in Table 2 indicate that sample 4 has relatively high electrode reversibility. The differences $E_{OE}-E_O$ are taken as a measure of the performance of the electrode.[3] The higher $E_{OE}-E_O$ value of sample 4 allows the electrode made of this material to be charged fully before oxygen evolution and exhibit much better electrochemical-cyclic properties. Therefore, the zinc-substituted nickel hydroxide nanostructures show good electrode reversibility and could have major potential as positive-electrode materials.

Table 4. Reduction potential E_R, oxidation potential E_O, oxygen-evolution potential E_{OE}, E_O-E_R, and $E_{OE}-E_O$ for electrodes made from samples 2, 4, and 5 at 20 °C.

Sample	E_R [mV]	E_O [mV]	E_{OE} [mV]	E_O-E_R [mV]	$E_{OE}-E_O$ [mV]
2	420	611	700	191	89
4	455	553	709	98	156
5	435	549	593	114	44

Conclusions

Zinc-substituted nickel hydroxide nanostructures have been synthesized for the first time from the flakelike nanostructured precursor $Zn_5(OH)_8Cl_2{\cdot}H_2O$ by the so-called coordinative homogenous precipitation method. By simply adjusting the initial experimental conditions, we can effectively control the structure, morphology, and chemical composition of the zinc-substituted nickel hydroxide nanostructures. Several parameters were found to play key roles in the formation of such structures: temperature, the amount of the ammonia, and the nature of the reactant. In this new method, although the zinc-substituted α-and β-nickel hydroxides have similar morphology to those previously reported, their growth process are different. The coordinative homogenous precipitation mechanism is used to explain the formation process of the zinc-substituted nickel hydroxide nanostructures formed in present reaction system. The zinc-substituted nickel hydroxide nanostructures have potential as multifunctional materials due to their interesting optical, magnetic, and electrical properties.

Experimental Section

Chemicals: All chemicals were purchased in analytical grade from Shanghai Chemical Reagents Company and used without further purification.

Preparation of $Zn_5(OH)_8Cl_2{\cdot}H_2O$ precursor: The precursor $Zn_5(OH)_8Cl_2{\cdot}H_2O$ can be easily synthesized by a simple and reproducible method. In a typical synthesis, 100 mL of 2 mol L^{-1} $ZnCl_2$ solution was added into a beaker and maintained at 80 °C in an electric oven for 3 h, during which it formed an ionic-liquid-like solution. Then, 25 mL of the $ZnCl_2$ solution was transferred to another beaker, and ethylenediamine (0.5 mL) was slowly dropped into it with magnetic stirring. A white precipitate formed, and the beaker was kept at 80 °C in an oven for a further 12 h. Finally, the white precipitate was filtered off, washed with double-distilled water several times, and dried in a vacuum oven at 60 °C for 3 h.

Preparation of zinc-substituted nickel hydroxide nanostructures: In a typical experiment, $Zn_5(OH)_8Cl_2{\cdot}H_2O$ (0.0440 g) and a suitable amount of $NiCl_2{\cdot}6H_2O$ were added to double-distilled water (42 mL). Then aqueous ammonia solution (3.5 mL, 25–28 wt %) was added to the mixed solution with stirring until the solution became clear. The solution was put into a 50 mL Teflon-lined autoclave. After being sealed, the autoclave was heated at 120 °C for 12 h. After hydrothermal treatment, the pale green or blue-green precipitate was separated from the solution by centrifugation, washed with doubly distilled water and absolute ethanol, and dried at 60 °C for 24 h in vacuo. The complete experimental results are summarized in the Supporting Information, Table S1.

Chemical stability of zinc-substituted nickel hydroxide nanostructures: The chemical stability of the synthesized nickel hydroxide samples was examined by immersing 0.5 g of powder in 6 M KOH solution at room

temperature for 40 days. After immersion, the products were collected by centrifugation, washed by deionized water and absolute ethanol, and dried at 60 °C for 24 h in vacuo.

Characterization: Powder X-ray diffraction (XRD) analyses were carried out on a Philips X'Pert PRO SUPER X-ray diffractometer equipped with graphite monochromatized $Cu_{K\alpha}$ radiation ($\lambda = 1.54056$ Å). Transmission electron microscopy (TEM) was performed on a Hitachi (Tokyo, Japan) H-800 transmission electron microscope at an accelerating voltage of 200 kV, and high-resolution TEM (HRTEM) on a JEOL-2011 operated at an acceleration voltage of 200 kV. EDX spectra were recorded with a JEOL-2011 transmission electron microscope. X-ray photoelectron spectroscopy (XPS) was preformed with an ESCALAB 250 X-ray photoelectron spectrometer (Thermo-VG Scientific). FTIR spectra were measured on a Bruker Vector-22 FTIR spectrometer. The UV/Vis/NIR spectra was recorded on a DUV-3700 absorption spectra (Shimadzu Corporation). Thermogravimetric analysis (TGA) was carried out on a TGA-50 thermal analyzer (Shimadzu Corporation) with a heating rate of 10 °C min^{-1} in flowing air. Dinitrogen adsorption was determined by BET measurements with an ASAP-2000 surface-area analyzer. Elemental analysis was performed by XRF-180 X-ray fluorescence spectrometry (Shimadzu Corporation). Photoluminescence (PL) spectroscopy was carried out at room temperature by using an He–Gd laser as excitation source and a double-grating monochromator connected to a photocounting system. The magnetic measurements on powdered samples enclosed in a medical cap were carried out at 4 K by using a commercial SQUID magnetometer (MPMS-XL) from Quantum Design Corp. The temperature-dependent magnetization was studied in an applied magnetic field of 100 Oe from 2 to 80 K.

Acknowledgements

This work was supported by the National Science Foundation of China (Nos. 50732006, 20621061, 20671085, 20325104, 2005CB623601), the Centurial Program of the Chinese Academy of Sciences, Anhui Development Fund for Talent Personnel, and Anhui Education Committee (2006Z027, ZD2007004-1), the Specialized Research Fund for the Doctoral Program (SRFDP) of Higher Education State Education Ministry, and the Partner-Group of the Chinese Academy of Sciences—the Max Planck Society.

[1] S. R. Ovshinsky, M. A. Fetcenko, J. Ross, *Science* **1993**, *260*, 176.
[2] A. K. Shukla, S. Venugopalan, B. Hariprakash, *J. Power Sources* **2001**, *100*, 125.
[3] F. S. Cai, G. Y. Zhang, J. Chen, X. L. Gou, H. K. Liu, S. X. Dou, *Angew. Chem.* **2004**, *116*, 4308; *Angew. Chem. Int. Ed.* **2004**, *43*, 4212.
[4] a) C. Faure, C. Delmas, M. Fouassier, P. Willmann, *J. Power Sources* **1991**, *35*, 249; b) C. Faure, C. Delmas, P. Willmann, *J. Power Sources* **1991**, *35*, 263; c) M. Kurmoo, P. Day, A. Derory, C. Estournes, R. Poinsot, M. J. Stead, C. J. Kepert, *J. Solid State Chem.* **1999**, *145*, 452; d) M. Taibi, S. Ammar, N. Jouini, F. Fievet, P. Molinie, M. Drillon, *J. Mater. Chem.* **2002**, *12*, 3238; e) M. Drillon, P. Panissod, *J. Magn. Magn. Mater.* **1998**, *188*, 93.
[5] D. G. Evans, D. A. Xue, *Chem. Commun.* **2006**, 485.
[6] B. H. Liu, S. H. Yu, S. F. Chen, C. Y. Wu, *J. Phys. Chem. B* **2006**, *110*, 4039.
[7] D. N. Yang, R. M. Wang, M. S. He, J. Zhang, Z. F. Liu, *J. Phys. Chem. B* **2005**, *109*, 7654.
[8] C. Tessier, L. Guerlou-Demourgues, C. Faure, A. Demourgues, C. Delmas, *J. Mater. Chem.* **2000**, *10*, 1185.
[9] a) L. Guerlou-Demourgues, C. Tessier, P. Bernard, C. Delmas, *J. Mater. Chem.* **2004**, *14*, 2649; b) M. Dixit, P. V. Kamath, J. Gopalakrishnan, *J. Electrochem. Soc.* **1999**, *146*, 79; c) C. Tessier, L. Guerlou-Demourgues, C. Faure, M. Basterreix, G. Nabias, C. Delmas, *Solid State Ionics* **2000**, *133*, 11.
[10] a) A. Sugimoto, S. Ishida, K. Hanawa, *J. Electrochem. Soc.* **1999**, *146*, 1251; b) Y. L. Zhao, J. M. Wang, H. Chen, T. Pan, J. Q. Zhang, C. N. Cao, *Int. J. Hydrogen Energy* **2004**, *29*, 889; c) J. X. Dai, S. F. Y. Li, T. D. Xiao, D. M. Wang, D. E. Reisner, *J. Power Sources* **2000**, *89*, 40.
[11] L. Demourguesguerlou, C. Delmas, *J. Power Sources* **1993**, *45*, 281.
[12] L. GuerlouDemourgues, L. Fournes, C. Delmas, *J. Electrochem. Soc.* **1996**, *143*, 3083.
[13] L. J. Yang, X. P. Gao, Q. D. Wu, H. Y. Zhu, G. L. Pan, *J. Phys. Chem. C* **2007**, *111*, 4614.
[14] M. Hu, L. X. Lei, *J. Solid State Electrochem.* **2007**, *11*, 847.
[15] R. Ma, Z. Liu, K. Takada, N. Iyi, Y. Bando, T. Sasaki, *J. Am. Chem. Soc.* **2007**, *129*, 5257.
[16] P. Jeevanandam, Y. Koltypin, A. Gedanken, *Nano Lett.* **2001**, *1*, 263.
[17] E. Uzunova, D. Klissurski, S. Kassabov, *J. Mater. Chem.* **1994**, *4*, 153.
[18] Z. P. Xu, H. C. Zeng, *Chem. Mater.* **1999**, *11*, 67.
[19] M. J. Avena, M. V. Vazquez, R. E. Carbonio, C. P. Depauli, V. A. Macagno, *J. Appl. Electrochem.* **1994**, *24*, 256.
[20] L. Durandkeklikian, I. Haq, E. Matijevic, *Colloids Surf. A* **1994**, *92*, 267.
[21] J. Zhu, Z. Gui, Y. Ding, Z. Wang, Y. Hu, M. Zou, *J. Phys. Chem. C* **2007**, *111*, 5622.
[22] F. Portemer, A. Delahayevidal, M. Figlarz, *J. Electrochem. Soc.* **1992**, *139*, 671.
[23] G. J. D. A. Soler-Illia, M. Jobbagy, A. E. Regazzoni, M. A. Blesa, *Chem. Mater.* **1999**, *11*, 3140.
[24] C. Coudun, J. F. Hochepied, *J. Phys. Chem. B* **2005**, *109*, 6069.
[25] B. Liu, S. H. Yu, F. Zhang, L. J. Li, Q. Zhang, L. Ren, K. Jiang, *J. Phys. Chem. B* **2004**, *108*, 4338.
[26] a) L. S. Zhong, J. S. Hu, H. P. Liang, A. M. Cao, W. G. Song, L. J. Wan, *Adv. Mater.* **2006**, *18*, 2426; b) C. Burda, X. B. Chen, R. Narayanan, M. A. El-Sayed, *Chem. Rev.* **2005**, *105*, 1025; c) Y. Cheng, Y. S. Wang, Y. H. Zheng, Y. Qin, *J. Phys. Chem. B* **2005**, *109*, 11548; d) R. L. Penn, *J. Phys. Chem. B* **2004**, *108*, 12707; e) J. Park, V. Privman, E. Matijevic, *J. Phys. Chem. B* **2001**, *105*, 11630.
[27] Y. Y. Luo, G. H. Li, G. T. Duan, L. D. Zhang, *Nanotechnology* **2006**, *17*, 4278.
[28] M. Jobbagy, M. A. Blesa, A. E. Regazzoni, *J. Colloid Interface Sci.* **2007**, *309*, 72.
[29] A. Ludi, W. Feitknecht, *Helv. Chim. Acta* **1963**, *46*, 2226.
[30] M. Guillot, M. Richard-Plouet, S. Vilminot, *J. Mater. Chem.* **2002**, *12*, 851.
[31] M. Richard-Plouet, S. Vilminot, *J. Mater. Chem.* **1998**, *8*, 131.
[32] S. Rouba, P. Rabu, E. Ressouche, L. P. Regnault, M. Drillon, *J. Magn. Magn. Mater.* **1996**, *163*, 365.
[33] M. Kurmoo, C. J. Kepert, *New J. Chem.* **1998**, *22*, 1515.

Received: March 13, 2008
Revised: June 24, 2008
Published online: August 20, 2008

